A through-thickness damage regularisation scheme for shell elements subjected to severe bending and membrane deformations

Miguel Costas*, David Morin, Odd Sture Hopperstad, Tore Børvik, Magnus Langseth

Structural Impact Laboratory (SIMLab) and Centre for Advanced Structural Analysis (CASA), Department of Structural Engineering, Norwegian University of Science and Technology (NTNU), NO-7491 Trondheim, Norway

Abstract

This research work proposes and validates a damage regularisation model for shell elements used in large-scale simulations. The model evaluates the ratio of bending to membrane loading in the elements based on the through-thickness gradient of the through-thickness plastic strain. The Cockcroft-Latham failure criterion is adopted, whose parameters are modified according to the length-to-thickness ratio of the shell elements in order to reduce the mesh dependency. This regularisation scheme is validated against experimental component tests on a double-chamber profile in an AA6005-T6 recrystallised aluminium alloy under quasi-static and impact loading conditions. The results show that the model is able to accurately predict fracture initiation under all tested conditions.

Keywords: Shell elements, through-thickness regularisation, ductile fracture, mesh dependency, local necking.

1. Introduction

From aircraft components to bridge decks, shell elements are the industry's usual choice to model mid- to large-scale structural problems. They provide engineers with a robust idealisation of the stress space, enabling to efficiently tackle problems where two dimensions are larger than the third one. The versatility of this element type makes it suitable for a wide range of structural applications in thin-walled structures.

*Corresponding author.

Email addresses: miguel.costas@ntnu.no (Miguel Costas), david.morin@ntnu.no (David Morin), odd.hopperstad@ntnu.no (Odd Sture Hopperstad), tore.borvik@ntnu.no (Tore Børvik), magnus.langseth@ntnu.no (Magnus Langseth)

Whereas shell elements can be safely applied to problems involving elastic-plastic loading and unloading, the accurate prediction of damage and failure is still a challenge, especially for thin sheets. Like most ductile materials, metals will most likely experience strain localisation before failure, often in the form of a local neck in sheet metals. Two main issues hinder the correct capture of such phenomenon using shell elements: i) the element size is usually much larger than the neck, and ii) the evolution of the neck cannot be simulated with shells as long as the strain localisation turns into a triaxiality-driven problem where the six components of the stress and strain tensors play a significant role. The former implies that the finite element solution is dependent on the mesh size, whereby a finer discretisation increases the fracture strain. The latter implies that plane-stress conditions no longer apply and thus the problem cannot be accurately simulated with shell elements.

A literature review reveals some relevant contributions dealing with the previous points. A series of empirical relationships have been proposed to obtain the fracture strain as a function of the element dimensions (usually the length-to-thickness ratio). Most of them come from the field of marine engineering and ship collisions, where massive metallic structures are commonly modelled with large shell elements. Some of these are the Germanischer Lloyd criterion [1], Barba's law [2], or Ehler's formula [3]. Barba's relationship was adopted by Hogström et al. [4] in combination with a forming limit curve to predict failure in shell elements in terms of length scale and multiaxiality. Digital Image Correlation (DIC) was used in their tests for an accurate measurement of the displacement fields on the surface of the specimens. A concise work investigating the effects of the element size for three different stress states was published by Kõrgesaar et al. [5], where a method averaging the stresses and strains in a representative volume was used to extrapolate the values to larger elements, in combination with different instability criteria. Nevertheless, this work was limited to membrane loads only. A parallel work by the same authors validated the model predicting failure in indented panels [6]. Walters [7] proposed an approximate fracture locus dependent on the element size and the stress state to face the same problem. Aretz et al. [8] proposed a predictive model based on a combination of the Marciniak-Kuczyński [9] and Hill's necking criteria [10], assembled together in a forming limit curve affected by a factor to account for large elements. An extension

and experimental validation of the model was presented in [11], where the authors also pointed to the need of extending the models to account for bending loading. A different approach can be found in Andrade et al. [12], where the authors proposed also a regularisation of the fracture criterion based on the element size and the stress state. They proposed a damage variable dependent on the incremental plastic strain combined with an instability variable, which enabled to account for non-linear strain paths. A local instability criterion was also employed by Storheim et al. [13] based on a combination of Hill's [10] and Bressan-Williams [14] stress-based necking criteria to deal with ductile failure prediction in coarsely meshed structures. The combination of both criteria, previously proposed in [15], enabled to predict local necking in the first and second quadrants of the forming limit diagram.

The common shortcoming in the previously referenced works is that they present regularisation schemes limited to membrane loading. In general, a sheet metal shows a much higher structural ductility when subjected to bending than when membrane loads dominate, due to the fact that bending loads do not trigger any local necking. Thus, for a correct representation of this phenomenon, the ductility of each shell element in a model should be dependent on the ratio of bending to membrane loads that the element is subjected to. There are just a few studies in the literature where this issue is addressed. Stoughton and Yoon [16] proposed a method which combined a fracture predictor with a necking criterion employing a forming limit curve and a shear criterion. The novelty is that they made the model dependent on the through-thickness stress distribution in the elements to identify the failure mode. In a similar vein, a recent work by Pack and Mohr [17] introduced the concept of the "domain of shell-to-solid equivalence", a sort of forming limit diagram extended to non-proportional loading. This domain was established using the Marciniak-Kuczyński analysis [9], and the retardation of fracture due to predominant bending loads was accounted for with a through-thickness evaluation of a necking criterion. The results were compared with additional simulations using a fine solid element mesh.

In this study, a through-thickness damage regularisation model for shell elements (TTR) is proposed with two main objectives: to compute failure as a function of the bending-to-membrane loading ratio of each element, and to reduce the mesh dependency of the failure strain under membrane loading. The bending-to-membrane load-

ing ratio is computed using the through-thickness variation of the through-thickness plastic strain. The model is validated against experimental tests, where a variety of loading scenarios is studied.

2. Formulation of the damage regularisation model

The Cockcroft-Latham (C-L) fracture criterion [18] was adopted in this investigation. It is worth highlighting that this choice implies no loss of generalisation since the formulation of the regularisation strategy is independent of the failure criterion adopted to compute the damage variable. The C-L criterion defines the damage variable D as

$$D = \int \frac{1}{W_{\mathrm{C}}} \langle \sigma_{\mathrm{I}} \rangle \, \mathrm{d}p, \tag{1}$$

where W_{C} is an experimentally determined parameter, σ_{I} is the major principal stress, $\langle \sigma_{\mathrm{I}} \rangle = \max \{\sigma_{\mathrm{I}}, 0\}$, and p is the equivalent plastic strain. Failure occurs at an integration point when the damage variable reaches a value of 1. Despite its simplicity, the C-L criterion has been proved reliable under a wide range of complex loading conditions, such as ballistic penetration [19, 20] and blast-loaded sandwich and thin panels [21, 22].

If the Cockcroft-Latham damage model is adopted in a mesh of fine solid elements, failure is exclusively governed by the parameter W_{C} which is calibrated using a tensile test. The mesh of sufficiently small solid elements should be able to reproduce the necking of the metal sheet and its failure when the damage variable defined in Equation (1) reaches a value of 1, regardless of the loading state. Thus, if small solid elements are used, the C-L parameter can be considered an intrinsic mechanical property of the material governing its ductility.

The main disadvantage of using solid elements in simulations of sheet metals under large deformations is that a very large number of elements is required to capture necking correctly. Therefore, this solution is not usually suitable for industrial-scale simulations due to the elevated computation times. Shells are commonly preferred in this case, with an element size usually larger than the neck. This implies that necking cannot be properly simulated, thus it is necessary to artificially reduce the ductility of those elements in areas susceptible to experience local necking.

Figure 1 illustrates the principle of the proposed regularisation model. Carrying

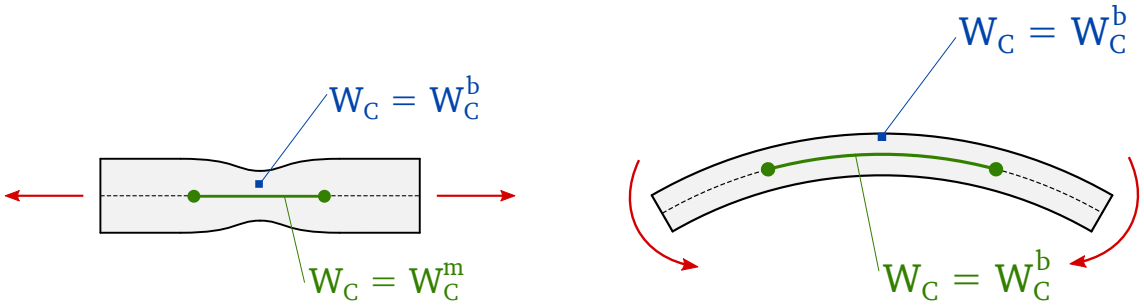

(a) (b)

Figure 1: Cockcroft-Latham parameters under pure membrane (a) and pure bending loading (b) for fine solid elements (blue) and shell elements (green).

out inverse modelling of a tensile test until fracture using fine solid elements (represented in blue in Figure 1a) gives the material's C-L parameter. This parameter will also determine when fracture is initiated under pure bending using solid elements, Figure 1b. On the other hand, if shell elements are used (represented in green) the value of the C-L parameter obtained from the inverse modelling of the tensile test using solid elements is only valid for cases without local necking, for instance under pure bending, Figure 1b. Therefore, this C-L parameter is hereinafter referred to as W_C^b, where the superindex "b" indicates that it governs failure in shell elements subjected to pure bending.

For shell elements under pure membrane loading, where the material can experience local necking, the C-L parameter W_C^m is assumed to be a function of the element's aspect ratio l_e/t_e, governed by the following exponential decay expression [23]:

$$W_C^m = W_C^l + \left(W_C^s - W_C^l\right) e^{\left(-c\left(\frac{l_e}{t_e}-1\right)\right)}, \tag{2}$$

where W_C^l, W_C^s, and c are fitting parameters to be obtained experimentally following the procedure explained in the next section.

In the areas under a combination of bending and membrane loading, the element ductility is balanced according to the following equation:

$$W_C = \Omega W_C^b + (1-\Omega)\, W_C^m. \tag{3}$$

In order to determine the relative amount of bending and membrane loading an element is subjected to, the deformation mode indicator Ω is introduced. It is defined

in terms of the through-thickness plastic strain of each element as

$$\Omega = \frac{1}{2}\frac{\left|\varepsilon^{\mathrm{T}}_{\mathrm{p},33} - \varepsilon^{\mathrm{B}}_{\mathrm{p},33}\right|}{\left|\max\left\{\varepsilon^{\mathrm{T}}_{\mathrm{p},33}, \varepsilon^{\mathrm{B}}_{\mathrm{p},33}\right\}\right|}, \tag{4}$$

where $\varepsilon^{\mathrm{T}}_{\mathrm{p},33}$ and $\varepsilon^{\mathrm{B}}_{\mathrm{p},33}$ are the through-thickness plastic strains at the top and bottom integration points of the element, respectively. It is straightforward to see that Ω takes a value of 1 under pure bending loading and 0 under pure membrane loading. Note that a corotational coordinate system is assumed where the x_3-axis is aligned with the thickness direction of the shell element. With this definition of the deformation mode indicator, the regularisation model is well suited for problems involving low to moderately non-proportional load paths. If a rate formulation were adopted instead, using the through-thickness plastic strain rate, the model would be able to capture severe or sudden changes in the load paths. However, after some benchmarking, a rate form was discarded because the elevated noise levels affected the quality of the results when large shell elements were used.

Therefore, whereas the C-L parameter under pure bending $W^{\mathrm{b}}_{\mathrm{C}}$ is assumed to be constant and intrinsic to the material, the determination of the structural ductility under pure membrane loading $W^{\mathrm{m}}_{\mathrm{C}}$ is a mesh-dependent problem. Thus, the C-L parameter W_{C} of each element is assumed here to be a function of the deformation mode.

Obtaining the fitting parameters $W^{\mathrm{l}}_{\mathrm{C}}$, $W^{\mathrm{s}}_{\mathrm{C}}$, c, and the C-L parameter under pure bending $W^{\mathrm{b}}_{\mathrm{C}}$ requires tensile testing, digital image correlation (DIC), and some simple numerical models. The procedure is fully developed in the next section. In this study, the TTR model was implemented in Abaqus/Explicit through a VUMAT user-defined subroutine.

The effect of regularising the damage parameters can be observed by plotting the fracture loci for pure bending ($\Omega = 1$) and pure membrane loads ($\Omega = 0$). Figure 2 shows both fracture loci for the AA6005-T6 alloy used in the present study, with the pure membrane curve particularised for $l_{\mathrm{e}}/t_{\mathrm{e}} = 1$.

3. Material tests and constitutive modelling

The proposed regularisation method was calibrated and validated against a series of experimental tests on components built from a double-chamber profile in an AA6005-T6 recrystallised aluminium alloy, provided by Hydro Extruded Solutions. This section

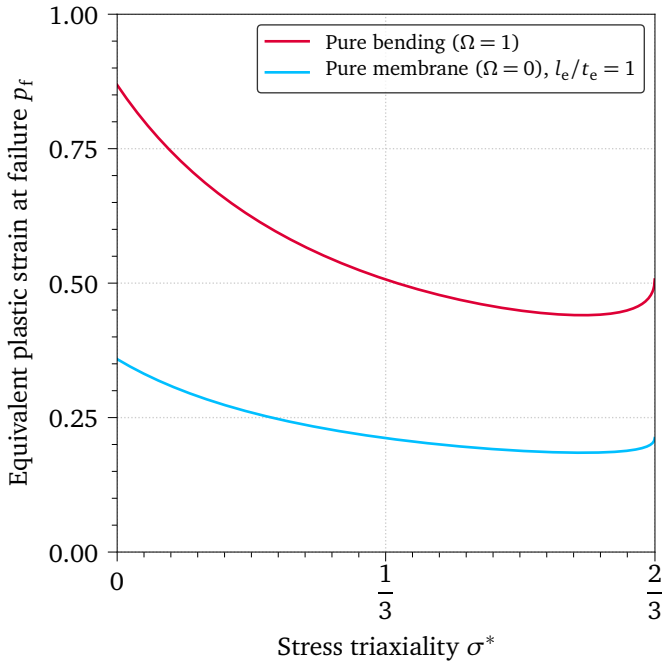

Figure 2: Fracture loci under pure bending and pure membrane loading using the current regularisation model for the studied AA6005-T6 alloy.

elaborates on the material testing and constitutive modelling, including the calibration of the regularisation model.

3.1. Extrusion welds and microstructure of the profile

The tested aluminium profiles presented a recrystallised texture stemming from the thermomechanical history along the production process. Extrusion welds were formed during the conformation of the profile, which could lead to a variation in the material properties. The cross-section of the profile is provided in Figure 3a, where the location of the extrusion welds is indicated. A study consisting of a metallographic analysis and Vickers hardness tests was conducted in order to detect and quantify possible variations in the microstructure of the material or in its hardness. To that end, material samples were extracted from the three weld locations – top flange, side wall and inner wall – and from the matrix material. These samples were conveniently ground, electro-polished and anodised before being analysed using light microscopy. The metallographic pictures revealed some minor differences in terms of grain orientations comparing the extrusion welds and the base material, as depicted in Figures 4a and 4b. The Vickers hardness tests with evenly spaced indentations separated at 750 µm (Figure 4c) and a load of 1 kg showed no relevant difference between the

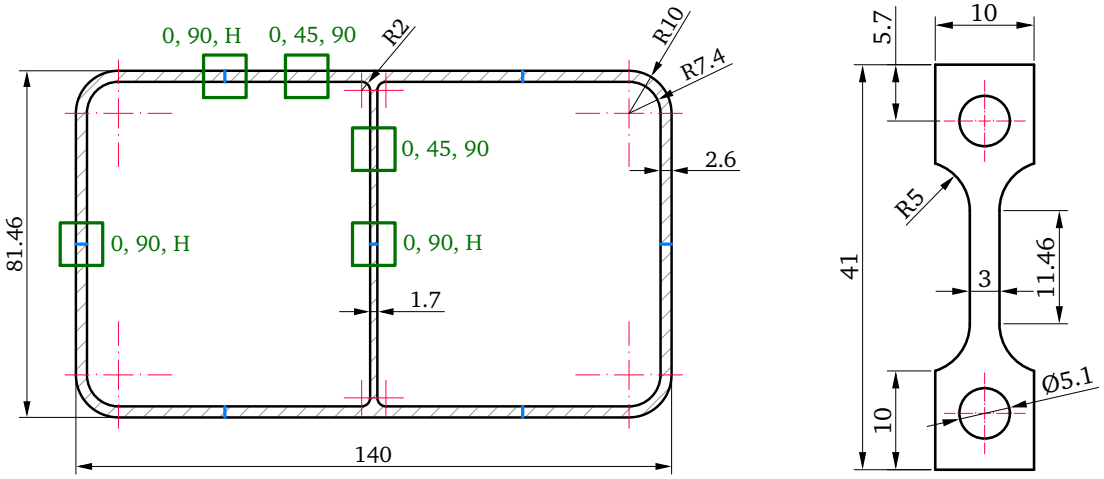

Figure 3: Dimensions of the cross-section (a) and the tensile specimens (b), at different scales. Extrusion welds are located at the blue markers. Green squares indicate the sample extraction areas. Extraction angles are provided with respect to the extrusion direction, and an "H" indicates the extraction of a hardness / metallographic specimen. Dimensions are in mm and angles in degrees.

material at the extrusion weld and the base material, with values ranging from 100 to 110 HV, see Figure 4c.

3.2. Extraction and testing of tensile specimens

An extensive testing campaign was carried out in order to characterise the mechanical properties of the recrystallised AA6005-T6 alloy. Tensile specimens with the dimensions provided in Figure 3b were extracted at different areas of the profile and at different orientations with respect to the extrusion direction, as shown in Figure 3a. Additional specimens were also extracted at the extrusion welds, with orientations of 0 degrees (along-weld) and 90 degrees (cross-weld), the extrusion welds being centred in both cases. Four tensile specimens were extracted at each location and orientation shown in Figure 3a, which led to a total of 48 tensile specimens. Special care was taken to avoid overheating the material during the extraction of samples. Thus, the specimens were extracted using a cutting wire inside a pool of water.

All tensile tests were carried out at 0.67 mm/min, and recorded with a Prosilica GC2450 camera at 2 frames per second with an approximate resolution of 140 px/mm. A black-and-white speckle pattern was painted on the specimens to enable the meas-

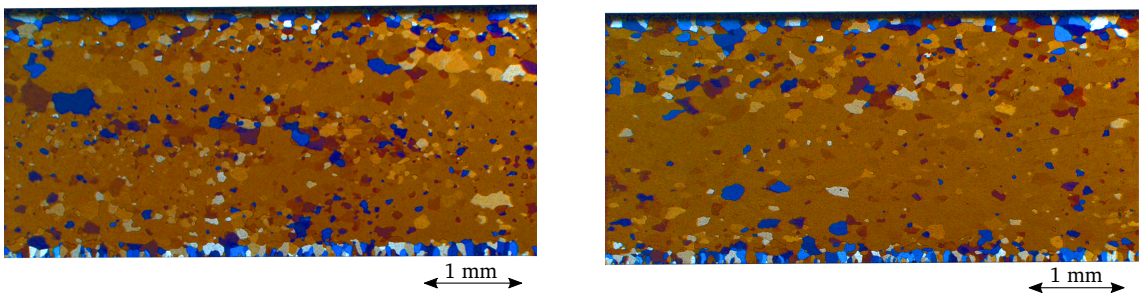

(a) (b)

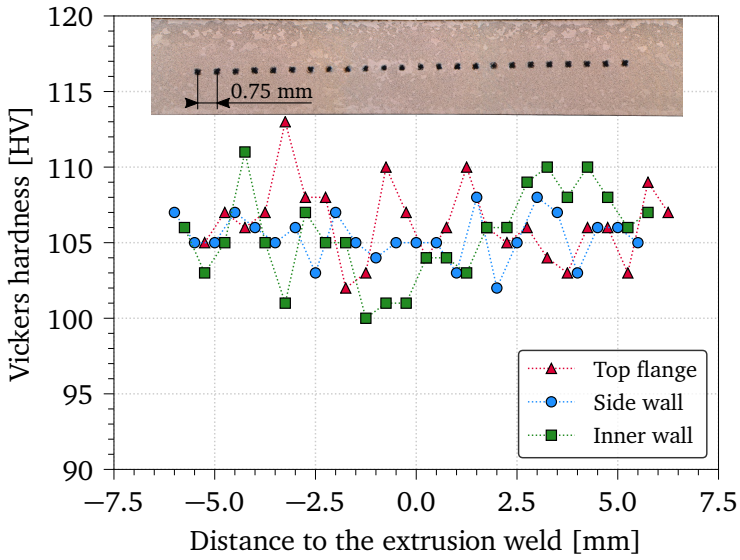

(c)

Figure 4: Metallographic photographs of the alloy at an extrusion weld (a) and the base material (b). The location of the hardness tests at one of the extrusion welds and the hardness measurements are provided in (c).

urement of surface strains using digital image correlation (DIC). This was preferred to an extensometer due to the small size of the specimens. Moreover, DIC provided the strain field over the whole surface of the gauge, revealing any possible effects of the extrusion welds. The in-house software eCorr was used for all the DIC analyses [24, 25].

The measured stress-strain curves are provided in Figure 5. Engineering strains were measured using a virtual extensometer on the DIC results. As stated, four repetitions were run for each test, even though only three are included in the plots for a neater display. Some differences were observed in the values of the initial yield stress for the different directions, whereas the work hardening was similar in all orientations. Compared to the specimens extracted from the base material, the along-weld specimens exhibited a somewhat higher initial yield stress, similar hardening, and earlier diffuse necking. The cross-weld specimens displayed a somewhat lower yield strength, higher strain hardening and earlier diffuse necking than the along-weld specimens. It was also observed that the stress ratios were different for the material at the top flange and the inner wall of the profile: the initial yield stresses at 0 and 45 degrees were similar at the top flange, whereas the initial yield stress at 45 degrees dropped for the material at the inner wall, matching the one for 90 degrees. In terms of the flow stress, the material exhibited only limited anisotropy due to the recrystallization process.

The plastic strain ratios (or Lankford coefficients) of the alloy were obtained by taking pre- and post-mortem measurements of the thickness and width of the tensile specimens from the base material, discarding the necks. These coefficients are defined as the ratio between the plastic strains in the width and thickness directions. Their values are provided in Table 1 for the three tested directions (0, 45, and 90 degrees with respect to the extrusion direction). From the variation of the plastic strain ratio with tensile direction, it is evident that the material has a strong plastic anisotropy, which is not seen in the flow stress curves.

The observation of the strain fields computed with digital image correlation on the surface of the tensile specimens showed that the increase in work hardening across the extrusion welds caused strains to concentrate away from the weld line, at a distance of approximately 3 mm measured from the extrusion weld. This was observed in all

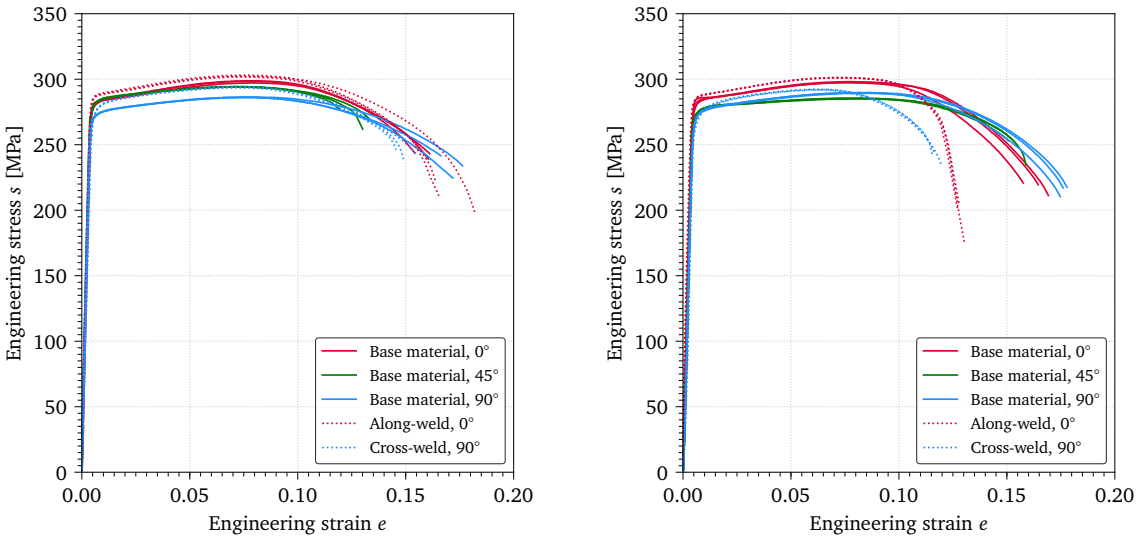

Figure 5: Engineering stress-strain curves of the aluminium alloy at the top flange (a) and inner wall (b) of the profile. Strains were measured using digital image correlation.

Table 1: Plastic strain ratios of the AA6005-T6 recrystallised alloy used in this study.

Location	R_0	R_{45}	R_{90}
Outer flange	0.578	0.159	2.386
Inner wall	0.554	0.111	2.134

the repetitions of the tensile tests on specimens with a weld crossing their gauges transversely. However, those specimens with the weld located longitudinally did not show any differences in the strain field compared to specimens extracted outside the welds. Figure 6 shows the contour plots of the first principal logarithmic strain over the surface of a cross-weld specimen and an along-weld specimens. The influence of the weld line can be clearly appreciated in the cross-weld specimen.

3.3. Material modelling

Given the relatively low flow stress anisotropy exhibited by the alloy in the tensile tests, the material was modelled as isotropic. This presented the advantage of a significant reduction of the computation times compared to an anisotropic yield surface, and also kept the present study orientated to a direct industrial application. Further-

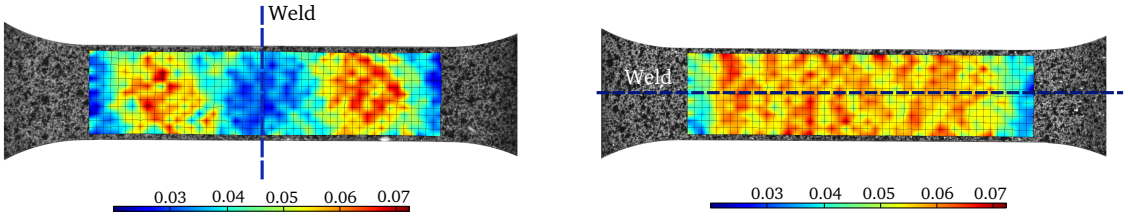

(a) Cross-weld specimen.

(b) Along-weld specimen.

Figure 6: First principal logarithmic strain fields before necking in tensile specimens extracted at the welds, obtained using digital image correlation.

more, no amendments were considered regarding the extrusion welds as long as the material behaviour was similar to that of the base material.

The tensile tests at the extrusion direction in the upper flange of the profile were taken as representative. A hypo-elastic plastic constitutive model was adopted to represent the material's behaviour. An elastic modulus of 70 GPa and a Poisson's ratio of 0.33 were assumed. The yield function f can be written as

$$f = \sigma_{\text{eq}} - (\sigma_0 + R) \leq 0, \tag{5}$$

where σ_{eq} is the equivalent stress, σ_0 represents the initial yield stress, and R is the isotropic hardening. The Hershey–Hosford yield criterion for isotropic plasticity was employed, which defines the equivalent stress as

$$\sigma_{\text{eq}} = \left[\frac{1}{2}\left(|\sigma_1 - \sigma_2|^m + |\sigma_2 - \sigma_3|^m + |\sigma_3 - \sigma_1|^m\right)\right]^{\frac{1}{m}}, \tag{6}$$

where σ_1, σ_2, and σ_3 are the principal stresses, and m defines the shape of the yield surface. The customary value of $m = 8$ was adopted, as it is recommended in the literature for FCC alloys [26]. The associated flow rule was adopted. Work hardening R was governed by an extended Voce law with three pairs of terms, reading

$$R = \sum_{i=1}^{3} Q_i \left[1 - \exp\left(-\frac{\theta_i}{Q_i} p\right)\right], \tag{7}$$

where Q_i represent the saturation stresses, θ_i are the initial hardening moduli, and p is the equivalent plastic strain.

The parameters were fitted to the experimental hardening curves using inverse modelling run in Abaqus/Standard [27] under an LS-OPT [28] framework, which

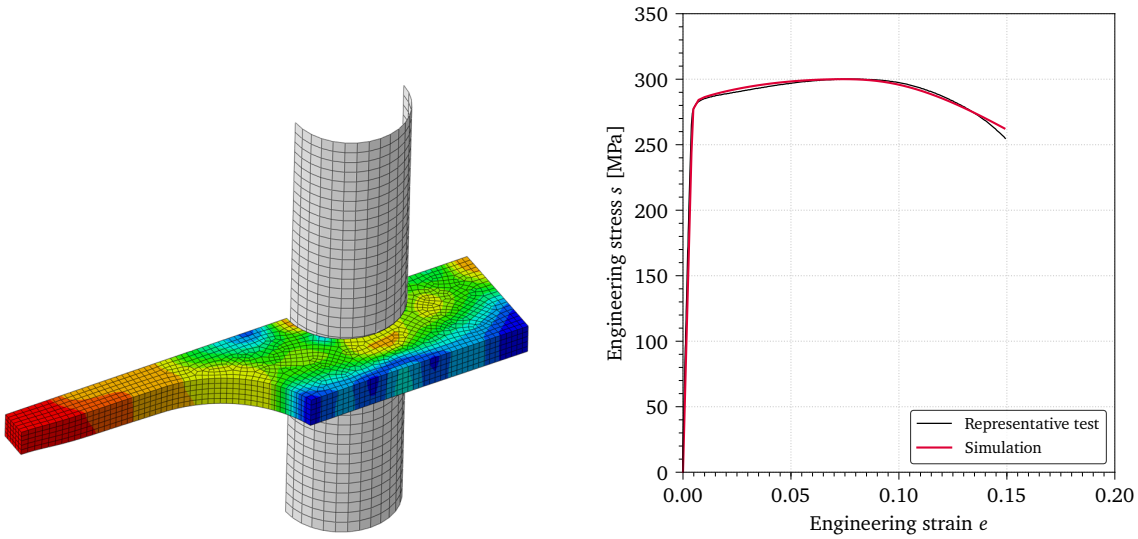

(a) (b)

Figure 7: Finite element model of one octave of the tensile specimen (a) and engineering stress–strain curves of the experimental representative test and the numerical simulation (b).

enabled the capture of the post-necking behaviour. Taking advantage of the symmetry of the specimen, only one octave of the coupon was modelled enforcing the pertinent boundary conditions. Solid elements with an element size of 0.26 mm were used in the numerical model, which implied 10 elements through the thickness of the specimen, see Figure 7a. The resulting numerical stress–strain curve is compared with the experimental data in Figure 7b, and the parameters of the extended Voce hardening law can be found in Table 2.

Table 2: Parameters of the extended Voce hardening rule, given in MPa.

σ_0	Q_1	θ_1	Q_2	θ_2	Q_3	θ_3
275.7	8.610	7095	48.47	702.3	12.16	166.3

The damage model based on the proposed regularisation scheme requires a series of parameters as input, which were also obtained from the tensile tests. The C-L parameter under pure bending $W_{\mathrm{C}}^{\mathrm{b}}$ determines the onset of failure without local necking. It was obtained running the finite element model with solid elements presented in Figure 7a in Abaqus/Explicit, with a time scaling factor of 25 000. Even though local

necking occurs in the simulation, the element discretisation is much smaller than the size of the neck, so it was reasonable to assume that the elements inside the neck can provide the $W_{\mathrm{C}}^{\mathrm{b}}$ parameter, assumed to be a material property. Given that a direct observation of the tensile tests does not allow to determinate the point where fracture initiates inside the specimen, this point had to be estimated using an iterative approach. LS-OPT was used to obtain the C-L parameter which produced a crack propagating from the centre of the specimen and reaching the specimen's surface at the same point as in the experimental tensile tests. A value of $W_{\mathrm{C}}^{\mathrm{b}} = 170.50\,\mathrm{MPa}$ was obtained this way.

The Cockcroft-Latham parameter under pure membrane loading $W_{\mathrm{C}}^{\mathrm{m}}$ depends on the element length-to-thickness ratio, as previously explained (Equation (2)). This exponential relationship is driven by three parameters $W_{\mathrm{C}}^{\mathrm{l}}$, $W_{\mathrm{C}}^{\mathrm{s}}$, and c, which were fitted in a way similar to what was done by Morin et al. [23] and Hogström et al. [4]. To this end, vectors with different lengths l_{e} were placed at the necking region of the DIC images of the tensile tests. Their elongations were tracked and applied as boundary conditions to single shell elements of the same sizes l_{e}, loading them under uniaxial tension until the point when fracture took place in the experimental test. The Cockcroft-Latham parameters for the different element sizes were determined by numerical integration. Equation (2) was fitted to these results, leading to $W_{\mathrm{C}}^{\mathrm{l}} =$ 38.05 MPa, $W_{\mathrm{C}}^{\mathrm{s}} =$ 68.16 MPa, and $c =$ 1.388. This fit is graphically shown in Figure 8.

4. Validation tests and numerical simulations

4.1. Three-point bending tests

Three-point bending tests were performed on the extruded aluminium profile with an actuator speed of 10 mm/min to ensure quasi-static conditions. Polytetrafluoreten (PTFE) sheets with a thickness of 2 mm were placed between the components and the machine's actuator and supports to minimise friction, see Figure 9a. The actuator and the supports had a diameter of 60 mm and were machined of high-strength steel. The tests were run in an Instron 5985 machine and recorded with three Prosilica GC2450 cameras with a resolution of 2448×1164 px, one to track the displacement of the actuator using digital image correlation, and two to observe the crack initiation and

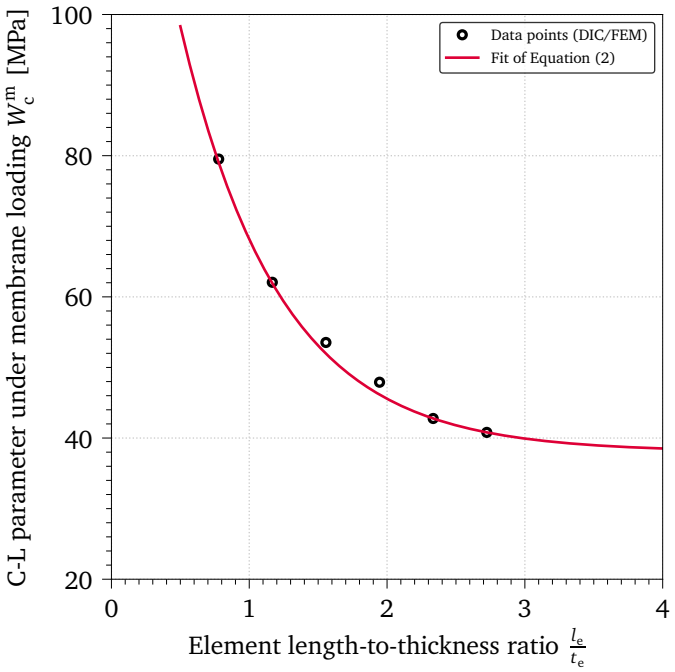

Figure 8: Mesh dependency of the Cockcroft-Latham parameter under pure uniaxial membrane loading W_C^m: data points and fit of Equation (2).

propagation. Five repetitions were run with components with notch (Figure 9b) and holes (Figure 9d), and four repetitions with the regular profile (without any notch or holes).

The experimental tests were modelled and simulated in Abaqus/Explicit using the previously described material model and the proposed damage regularisation strategy. Four-node shell elements with reduced integration and five through-thickness integration points were selected. Recall that only the outermost integration points are involved in the regularisation of the Cockcroft-Latham parameter. The parts were meshed with an approximate element size of 2.6 mm, both in the outer and the middle wall, resulting in approximate length-to-thickness ratios of 1.00 and 1.53, respectively. Special care was taken regarding the mesh size around the curved edges of the holes and notch, where a regular element shape was particularly enforced in order to have the same discretisation per unit arc length. The radii of the notch and the holes were intentionally the same and equal to 15 mm (Figures 9b and 9c). The averaged measured thicknesses, 2.570 mm and 1.733 mm, were employed in the simulations instead of the nominal values provided in Figure 3a. Even though the PTFE sheets were not modelled, their contribution was accounted for by assuming a constant fric-

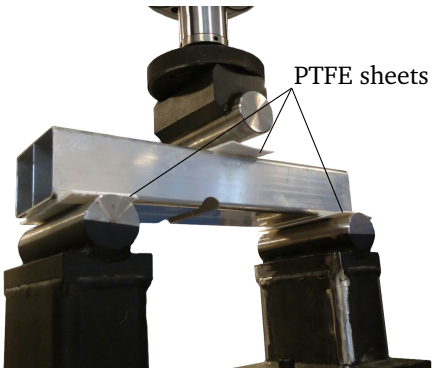

(a) Three-point bending set-up.

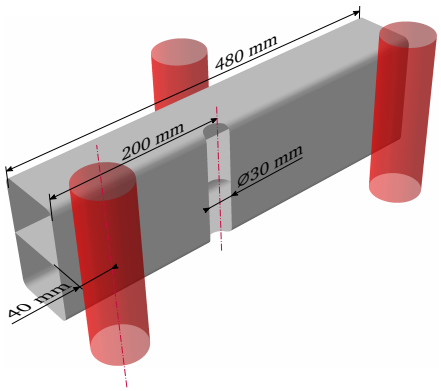

(b) 3PB component with notch.

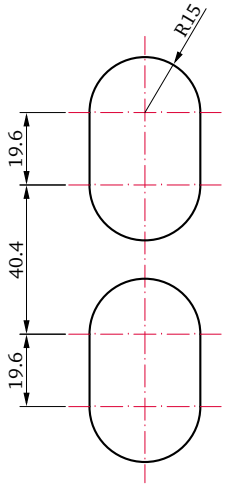

(c) Geometry of the holes.

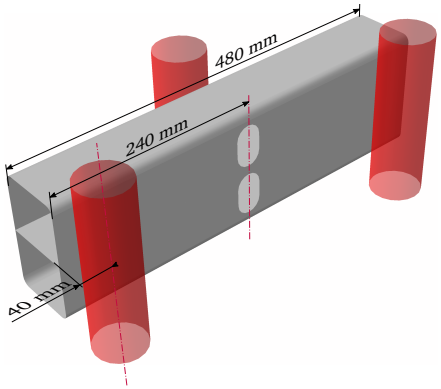

(d) 3PB component with holes.

(e) Axial crushing set-up.

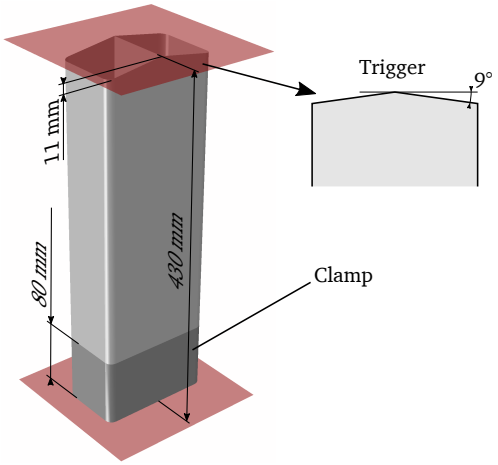

(f) Component for axial crushing.

Figure 9: Dimensions of the components, in millimetres, and experimental set-ups.

tion coefficient of 0.05. The actuators were modelled as perfectly rigid surfaces.

In order to get reasonable computation times, a time-scaling factor of 3000 was adopted in the simulations of the three-point bending tests. Quasi-static conditions were guaranteed through a smoothly ramped actuator speed and a check of the energy balance throughout the simulations.

Figure 10 shows a comparison between the experimental and numerical results of the three different three-point bending tests. Force-displacement curves are provided together with pictures of the post-mortem experimental components and the simulation contour plots of the deformation mode indicator Ω and the damage variable D. The plots of the deformation mode indicator clearly show which elements are undergoing damage under membrane or bending loads, or a combination of both. Notice that the deformation mode indicator was also computed in elements which did not experience plastic flow. For these elements, Ω was obtained using the total strain rate $\dot{\varepsilon}_{33}$, which produced some noise. In view of these results, the simulations are found to reproduce the experimental observations with a good degree of accuracy.

Also the fracture initiation was reasonably well predicted in the simulations, being slightly conservative in the case of the components with holes. This was due to the fact that the fillets connecting the middle and outer walls of the profile were not modelled, resulting in a minor loss of bearing capacity at the midpoint between both holes. As failure initiated there, earlier failure was predicted in the simulations compared to the experiments. To verify this, additional simulations were run where the thickness of the last row of elements in the middle wall was increased and then the failure point was exactly predicted.

The propagation direction of the crack in the components with a notch differed compared to the experimental observations. In the experiments the crack propagated from the notch towards the actuator, whereas in the simulations the propagation was mostly vertical. This was caused by the lattice geometry of the mesh, which facilitated the propagation along its two main directions rather than other directions. Nevertheless, the fracture initiation was correctly captured in the simulations, which was the goal of the regularisation scheme.

It is worth noticing that, in the case of the regular components, the middle wall buckled and a crack appeared at the top connection with the outer part of the profile

in two of the experiments, Figure 10a. Even though the corresponding elements in the model were damaged, Abaqus does not remove an element from the mesh until all its integration points fail, so no drop in the force-displacement curve was observed in the simulation.

4.2. Axial crushing tests

Axial crushing tests constitute a challenging validation scenario for the proposed fracture model, as they subject the profile to severe deformations and complex stress states. Quasi-static and impact axial crushing tests were conducted on components machined according to the dimensions displayed in Figure 9f, where the trigger at the top of the components was specifically designed to initiate a progressive collapse mode.

4.2.1. Quasi-static axial crushing tests

Components were firmly clamped to a rigid surface, as shown in Figures 9e and 9f. The clamping length was 80 mm in all cases, with two wooden blocks of the same length fitted inside the component to act as an inner clamp together with the outer hardware. The experimental tests were conducted at 10 mm/min to ensure quasi-static conditions, with a total crushing distance of 250 mm. A total of five repetitions were run in an Instron 5985 machine and recorded with two Prosilica GC2450 cameras with a resolution of 2448×1164 px, one of which tracked the axial displacement of the actuator.

These tests were simulated in Abaqus/Explicit with a configuration similar to that of the three-point bending tests, using an element size of 2.6 mm and linear shell elements with five through-thickness integration points and reduced integration. The actuator was modelled perfectly rigid and the clamp was simulated with a fixed boundary condition in the lower 80 mm of the part. A friction coefficient of 0.2 was assumed in these simulations. The time scaling factor was 25 000 for the axial crushing simulations in order to get a reasonable runtime. A smoothly ramped displacement of the actuator and a check of the energy balance ensured quasi-static conditions.

Figure 11 contains the force-displacement curves obtained from the experimental quasi-static tests and the simulations (Figures 11a and 11b), together with a photograph of the post-mortem components (Figure 11c) and two images of the simu-

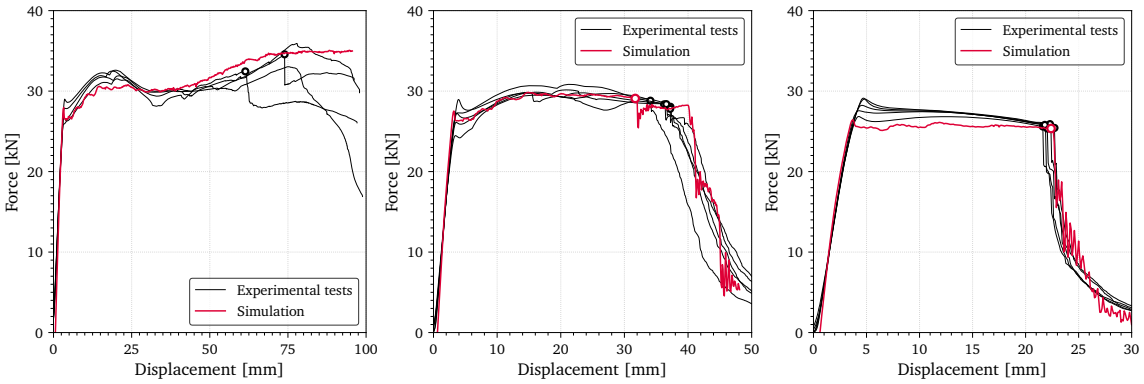

(a) Regular component. (b) Component with holes. (c) Component with notch.

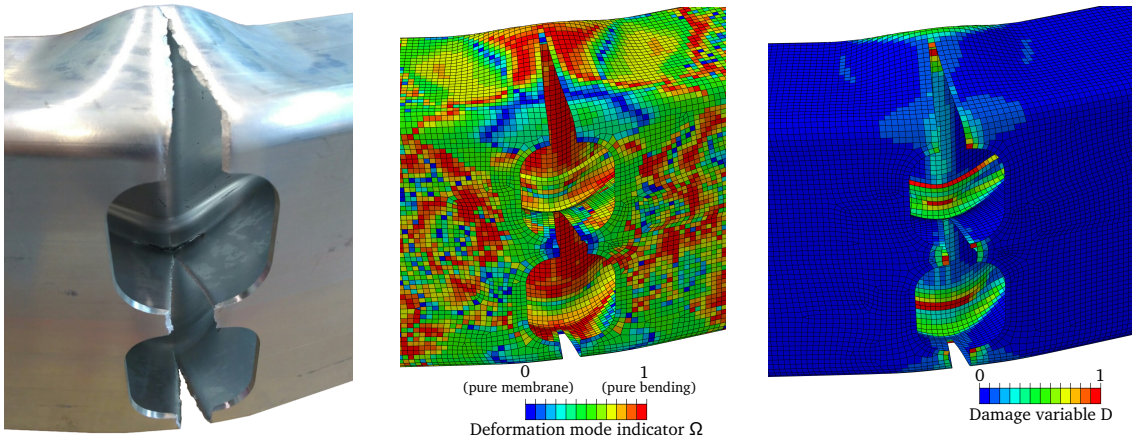

(d) (e) (f)

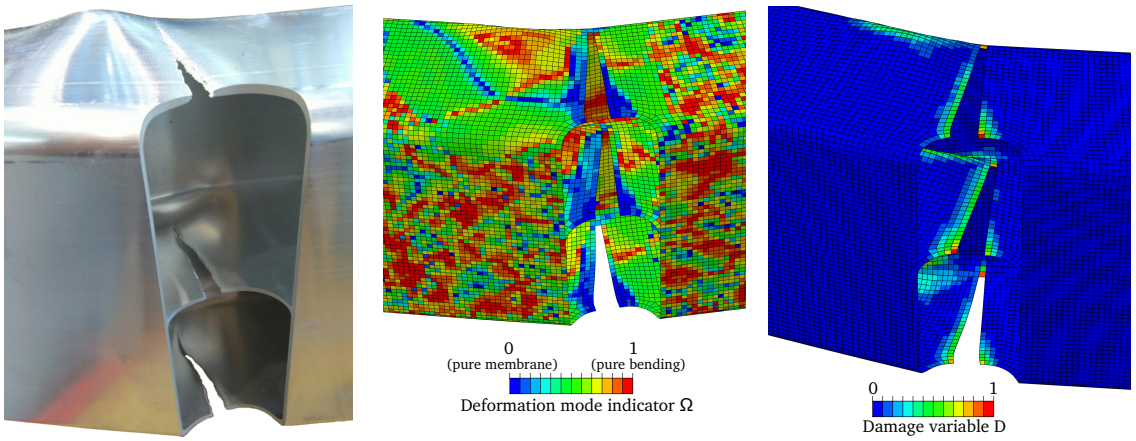

(g) (h) (i)

Figure 10: Comparison of the results of the experimental tests and the simulations. Figures (a) to (c) provide the force-displacement plots, where a dot represents the first fracture. Figures (d) to (i) show a representative post-mortem component and the simulation contour plots of the deformation mode indicator Ω and the damage variable D for the components with holes –(d) to (f)– and the components with a notch –(g) to (i).

lation results with colour maps of the deformation mode indicator Ω (Figure 11d) and the damage variable D (Figure 11e). In Figure 11b, the average force was obtained as a function of the axial crushing length, by computing the integral of the force-displacement curve $F(\delta)$ divided by the current displacement δ, as follows:

$$F_{\text{avg}}(\delta) = \frac{\int_0^\delta F(\delta)\,\mathrm{d}\delta}{\delta}. \tag{8}$$

The results show a rather good correlation between simulations and experiments, even though the forces measured in the simulations are 6 % higher than the average experimental value. Fracture was correctly captured in the numerical model, with some cracks at the corners of the profile and a continuous fracture along both ends of the middle wall. The latter caused the collapse mode of the profile to evolve from an asymmetric into a symmetric mode in both experiments and simulations, see Figure 12 for definition. Had the connections between middle and outer walls been strong enough to withstand the crushing, the asymmetric collapse mode would have prevailed through the whole process. Figure 12 illustrates how the tearing of the middle wall changed the global deformation mode to a symmetric pattern, with a lower energy absorption per unit length.

Figure 13 shows a comparison of the collapse modes in the numerical simulations with and without damage regularisation. The curvature of the folds in the case with regularisation (Figure 13a) is much more similar to what was observed in the experiments (Figure 12). The reason is the predominant bending loading of the elements in the folds. If the damage regularisation is disabled (Figure 13b), these elements experience an early failure. Enabling the regularisation prevents this early failure given that the value of the C-L parameter increases according to Equation (3).

4.2.2. Impact axial crushing tests

The same components were tested under impact loading in order to assess the effects of an increased loading rate on their behaviour, especially regarding fracture. Previous research has reported that profiles made of the same alloy can behave in a much more brittle way under impact loading compared to quasi-static tests [29, 30].

The impact tests were run using an in-house large pendulum accelerator dubbed “the kicking machine”, described thoroughly in [31]. This apparatus was proved re-

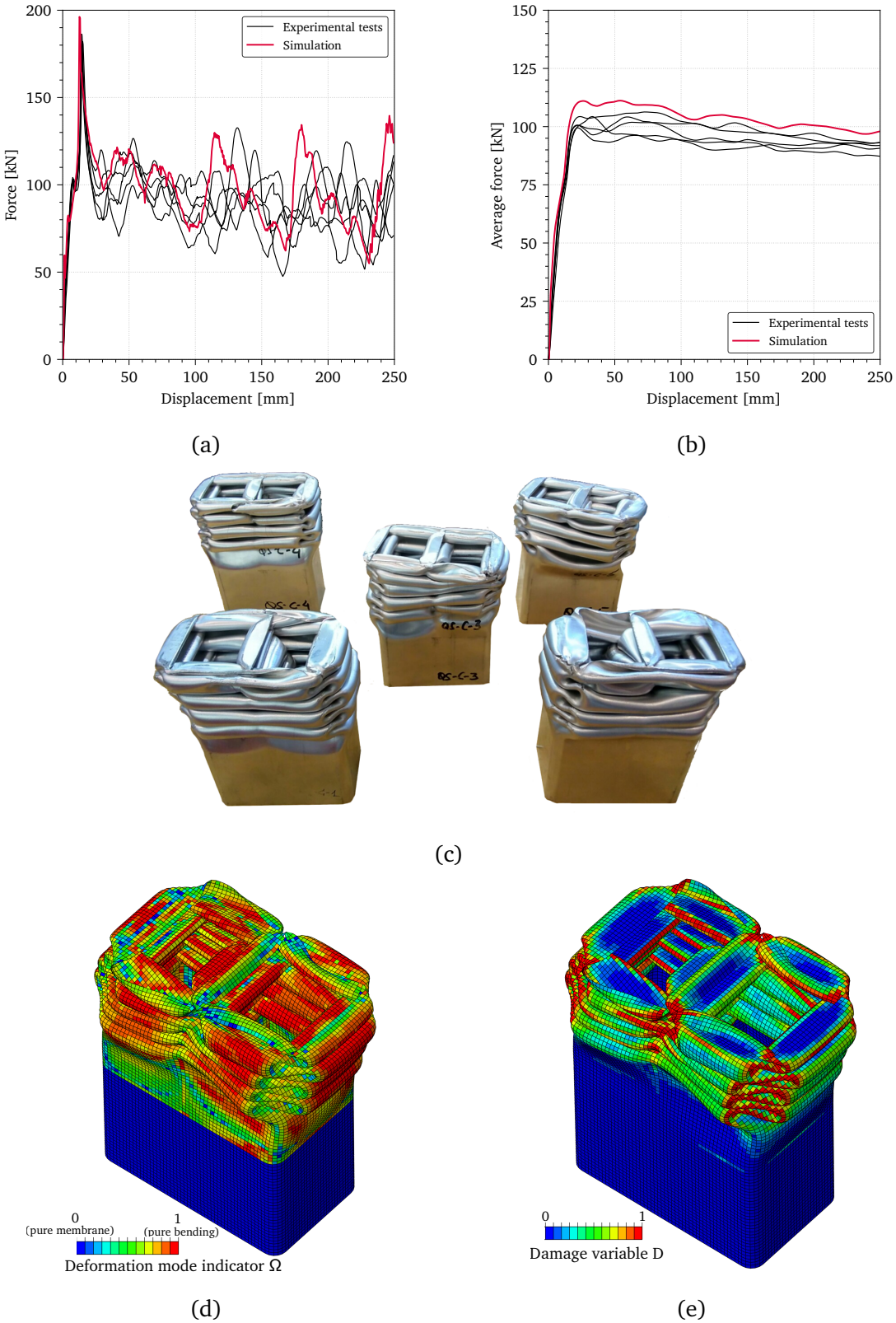

Figure 11: Quasi-static axial crushing tests. Comparison of the results obtained from the experimental tests and the simulation. Figures (a) and (b) provide the force-displacement and average force-displacement plots, respectively. Images of the post-mortem components are shown in (c), and figures (d) and (e) contain the simulation contour plots of the deformation mode indicator Ω and the damage variable D.

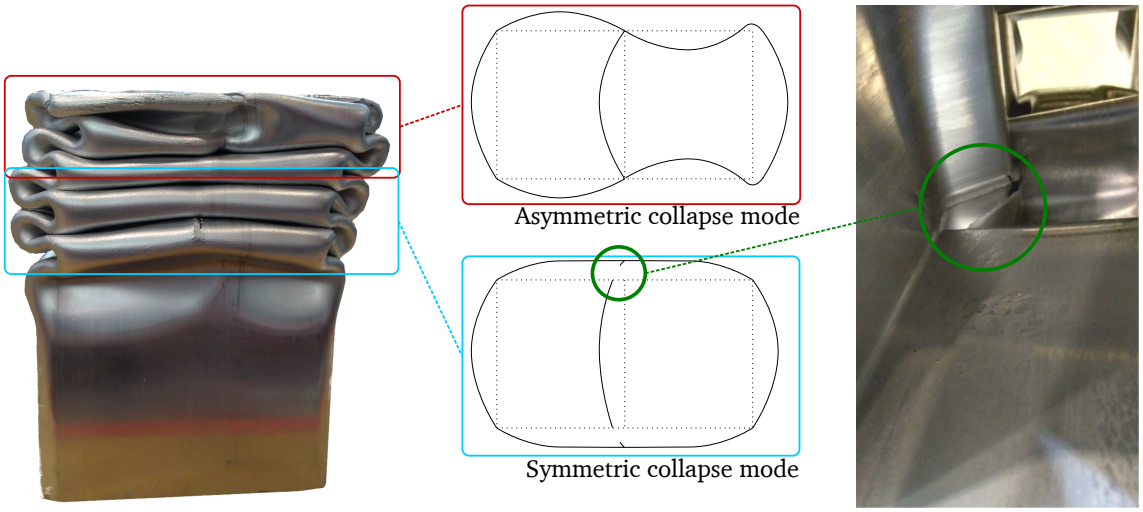

Figure 12: Transitional collapse mode observed in the axial crushing tests and simulations. The initiation of the asymmetric collapse mode was caused by the trigger, whereas the tearing of the middle wall at its corners caused the collapse mode to evolve into a symmetric pattern.

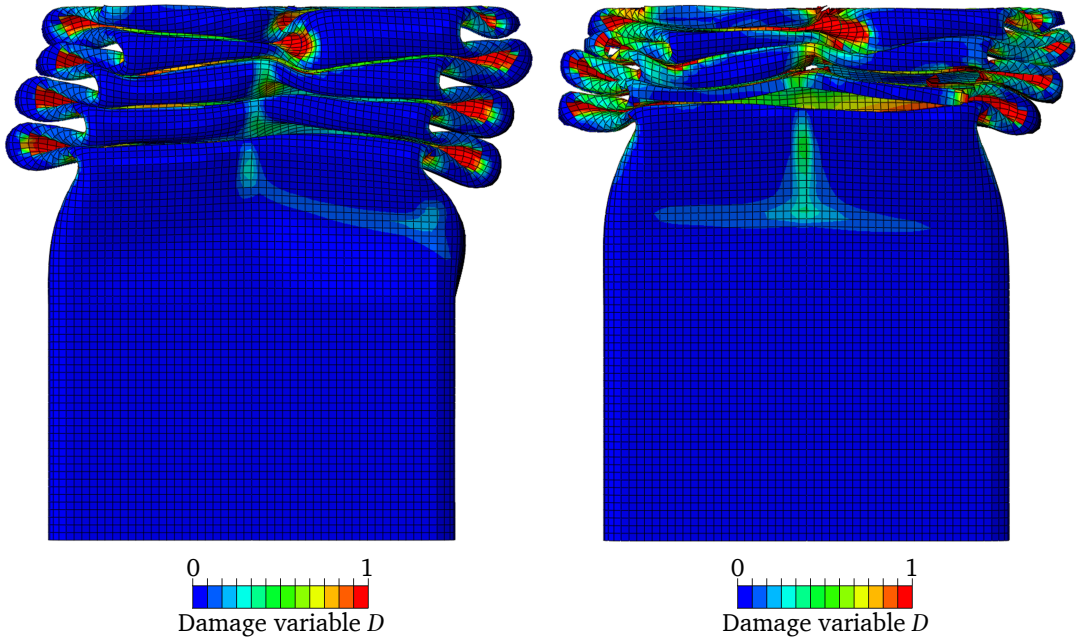

(a) (b)

Figure 13: Comparison between the folding pattern in the numerical simulations with regularisation (a) and without regularisation (b).

liable for a wide range of applications such as crash boxes [32, 33], stiffened panels [23], steel pipes [34] and, more recently, structural joints [35]. The components were fixed to a massive reaction wall with a mass of 150 tonnes using the same clamping system as the quasi-static tests. A trolley with a mass of 400 kg rolling on rails was accelerated up to an impact velocity of 11 m/s by a large hydraulic arm. The front of the trolley was equipped with a load cell designed for a maximum load of 500 kN. A pair of Photron Fastcam SA1.1 high-speed cameras recorded the tests at 250 000 frames per second. The number of repeat tests was five.

For the simulations, the same model as the one for the quasi-static tests was employed with the following modifications: time scaling was disabled, and the actuator was provided with a mass of 400 kg and an initial speed of 11m/s, replicating the test conditions. Simulations were run with and without strain rate sensitivity to assess its influence. In the case with strain rate sensitivity, this was accounted for using a Johnson-Cook term with C equal to 0.0082 and a reference strain rate of $\dot{\varepsilon}_0 = 1 \times 10^3\,\mathrm{s}^{-1}$ [36]. No relevant differences were found in the force-displacement curves or in the collapse modes, so the material was considered strain-rate independant for the current application. Due to this, any difference in the predicted force-displacement curves compared to the quasi-static simulations stems from the inertial effects. The force signals from the load cell and the simulations were filtered using a low-pass Butterworth filter to remove frequencies above 2 kHz, which is approximately the first natural frequency of the trolley according to [35].

The results of the experiments and the simulations are compared in Figure 14. An increased amount of damage in the components was observed compared to the quasi-static case. This increment was captured to a great extent in the simulations, as can be observed by comparing the contour plots of the damage variable for both cases, Figures 11e and 14e. Triggered by this increased damage, the collapse mode was more symmetric in the impact case than in the quasi-static. The model also predicted the force-displacement curves with a good degree of accuracy, as shown in Figures 14a and 14b.

4.3. Influence of the regularisation on the mesh sensitivity

One of the main objectives of the proposed damage regularisation is to reduce the mesh dependency in the prediction of fracture. Thus, a sensitivity study was carried

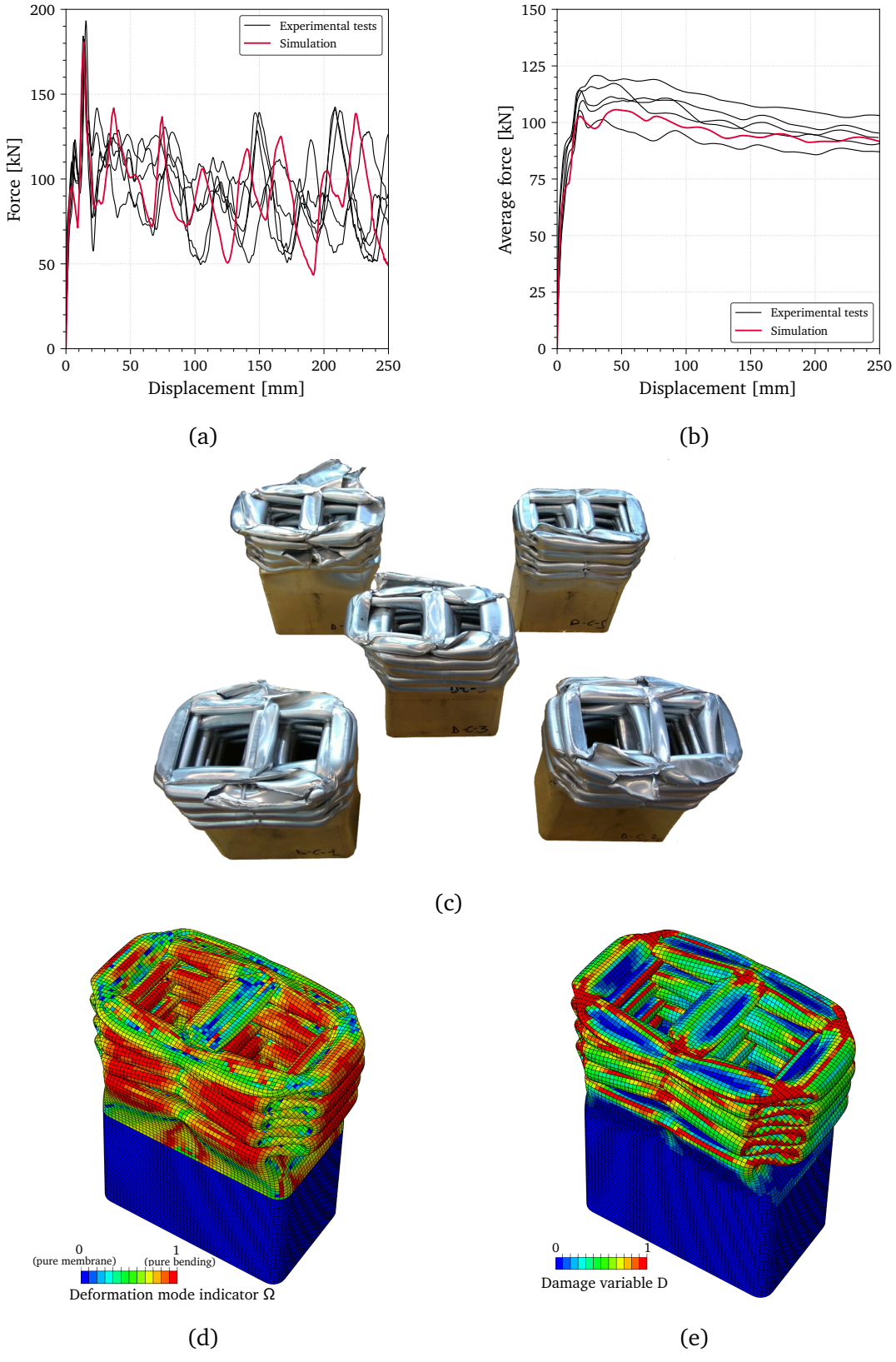

Figure 14: Impact axial crushing tests. Comparison of the results obtained from the experimental tests and the simulation. Figures (a) and (b) provide the force-displacement and average force-displacement plots, respectively. An image of the post-mortem components is shown in (c), and figures (d) and (e) contain the simulation contour plots of the deformation mode indicator Ω and the damage variable D.

out in order to quantify this effect in one of the validation tests. The three-point bending component with a notch was selected for this study.

The finite element model of the component was meshed using shell elements with a characteristic length of one, two, and three times the thickness of the outer plate, that is, 2.6, 5.2, and 7.8 mm. The designated element size was particularly enforced in the vicinity of the notch. The simulations were run with the same configuration as in the previous analyses and the following failure models were applied for each element size:

1. Regularised damage model (TTR)
2. Cockcroft-Latham fracture criterion with W_{C} calibrated for a shell size of 2.6 mm using DIC data as previously described, $W_{\mathrm{C}} = 69.12$ MPa.
3. Cockcroft-Latham fracture criterion using the W_{C} obtained from the simulation of the tensile tests with small solid elements, that is $W_{\mathrm{C}} = W_{\mathrm{C}}^{\mathrm{b}} = 170.50$ MPa.

The predicted displacements at the point where the first element is removed from the mesh are compared with the displacement at failure in the experimental tests in Figure 15. The reduction of the mesh sensitivity provided by the regularisation scheme can be clearly observed. It is also shown that the C-L criterion calibrated using the inverse modelling of the tensile tests with small solid elements overestimates the critical displacement to a large extent.

5. Conclusions

This work presents a regularisation strategy for damage modelling with shell elements, where the ductility of the elements is determined by their bending-to-membrane loading ratio. The following main conclusions can be drawn:

- The deformation mode indicator Ω defined in terms of the through-thickness plastic strain was found to be an adequate measure for evaluating the deformation mode of shell elements throughout the simulations. This implied that the regularisation could be formulated in a way independent of any damage criterion. The model was able to predict failure accurately in a variety of scenarios with complex loading involving local necking or severe bending of the material.

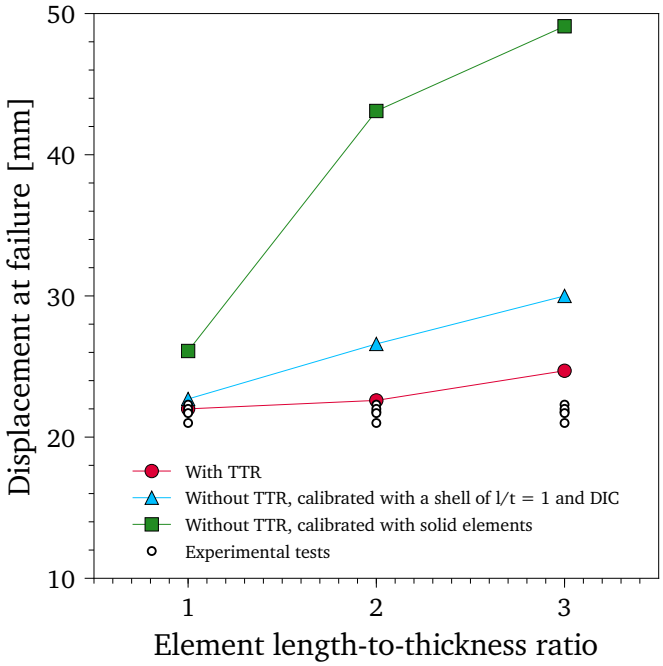

Figure 15: Comparison of the displacement at failure in the notched three-point bending experimental tests and the numerical predictions with and without the present damage regularisation model.

- The proposed scheme accounts for the different length-to-thickness ratios of all the elements in a finite element model providing a more realistic and less mesh-sensitive prediction of local necking.

- The formulation of the model was shown robust and relatively simple to implement in a commercial finite element code. The calibration of the through-thickness regularisation model was done using only one conventional tensile test and a software for digital image correlation.

- The predictions were validated against component tests loaded quasi-statically and under impact, with a good degree of accuracy.

6. Acknowledgements

The authors would like to acknowledge the financial support from the Centre for Advanced Structural Analysis (CASA) (Project No. 237885) funded by the Research Council of Norway and NTNU. The aluminium profiles used in this study were provided by Hydro Extruded Solutions. The help from Dr. Egil Fagerholt (NTNU)

and Dr. Jacobo Díaz (Universidade da Coruña) with the DIC batch-scripting is fully acknowledged. Some of the extensive experimental work was carried out by Mr. Alejandro Soriano, to whom the authors are grateful too. Credit for the priceless assistance at the lab must be given to Mr. Tore Wisth and Mr. Trond Auestad.

References

[1] M. Scharrer, L. Yhang, and E.D. Egge. Collision calculations in naval design systems. In *Final report MTK0614 No. ESS2002.183, Germanischer Lloyd*, Hamburg, Germany, 2002.

[2] Y. Yamada, H. Endo, and P. Terndrup-Pedersen. Numerical study on the effect of buffer bow structure in ship-ship collision. In *Proceedings of the 15th International Offshore and Polar Engineering Conference*, pages 604–611, Seoul, South Korea, 2005.

[3] S. Ehlers, J. Broekhuijsen, H.S. Alsos, F. Biehl, and K. Tabri. Simulating the collision response of ship side structures: A failure criteria benchmark study. *International Shipbuilding Progress*, 55 (1-2):127–144, 2008.

[4] P. Hogström, J.W. Ringsberg, and E. Johnson. An experimental and numerical study of the effects of length scale and strain state on the necking and fracture behaviours in sheet metals. *International Journal of Impact Engineering*, 36(10-11):1194–1203, 2009.

[5] M. Kõrgesaar, H. Remes, and J. Romanoff. Size dependent response of large shell elements under in-plane tensile loading. *International Journal of Solids and Structures*, 51(21):3752 – 3761, 2014.

[6] M. Kõrgesaar and J. Romanoff. Influence of mesh size, stress triaxiality and damage induced softening on ductile fracture of large-scale shell structures. *Marine Structures*, 38:1 – 17, 2014. ISSN 0951-8339.

[7] C. L. Walters. Framework for adjusting for both stress triaxiality and mesh size effect for failure of metals in shell structures. *International Journal of Crashworthiness*, 19(1):1–12, 2014.

[8] H. Aretz, S. Keller, R. Vogt, and O. Engler. Modelling of ductile failure in aluminium sheet forming simulation. *International Journal of Material Forming*, 4(2):163–182, 2011.

[9] Z. Marciniak and K. Kuczyński. Limit strains in the processes of stretch-forming sheet metal. *International Journal of Mechanical Sciences*, 9(9):609 – 620, 1967.

[10] R. Hill. On discontinuous plastic states, with special reference to localized necking in thin sheets. *Journal of the Mechanics and Physics of Solids*, 1(1):19 – 30, 1952.

[11] H. Aretz, S. Keller, O. Engler, and H.J. Brinkman. A simple ductile failure model with application to AA5182 aluminium sheet forming. *International Journal of Material Forming*, 7(3):289–304, 2014.

[12] F. X. C. Andrade, M. Feucht, A. Haufe, and F. Neukamm. An incremental stress state dependent damage model for ductile failure prediction. *International Journal of Fracture*, 200(1):127–150, 2016.

[13] M. Storheim, H.S. Alsos, O.S. Hopperstad, and J. Amdahl. A damage-based failure model for coarsely meshed shell structures. *International Journal of Impact Engineering*, 83:59 – 75, 2015.

[14] J.D. Bressan and J.A. Williams. The use of a shear instability criterion to predict local necking in sheet metal deformation. *International Journal of Mechanical Sciences*, 25(3):155 – 168, 1983.

[15] H.S. Alsos, O.S. Hopperstad, R. Törnqvist, and J. Amdahl. Analytical and numerical analysis of sheet metal instability using a stress based criterion. *International Journal of Solids and Structures*, 45(7):2042 – 2055, 2008.

[16] T. B. Stoughton and J. W. Yoon. A new approach for failure criterion for sheet metals. *International Journal of Plasticity*, 27(3):440 – 459, 2011.

[17] K. Pack and D. Mohr. Combined necking & fracture model to predict ductile failure with shell finite elements. *Engineering Fracture Mechanics*, 182:32–51, 2017.

[18] M. G. Cockcroft and D. J. Latham. Ductility and the workability of metals. *Journal of the Institute of Metals*, 96:33–39, 1968.

[19] T. Børvik, S. Dey, and A.H. Clausen. Perforation resistance of five different high-strength steel plates subjected to small-arms projectiles. *International Journal of Impact Engineering*, 36(7): 948 – 964, 2009.

[20] J.K. Holmen, J. Johnsen, O.S. Hopperstad, and T. Børvik. Influence of fragmentation on the capacity of aluminum alloy plates subjected to ballistic impact. *European Journal of Mechanics - A/Solids*, 55:221 – 233, 2016.

[21] H.N.G. Wadley, T. Børvik, L. Olovsson, J.J. Wetzel, K.P. Dharmasena, O.S. Hopperstad, V.S. Deshpande, and J.W. Hutchinson. Deformation and fracture of impulsively loaded sandwich panels. *Journal of the Mechanics and Physics of Solids*, 61(2):674 – 699, 2013.

[22] V. Aune, G. Valsamos, F. Casadei, M. Larcher, M. Langseth, and T. Børvik. Numerical study on the structural response of blast-loaded thin aluminium and steel plates. *International Journal of Impact Engineering*, 99:131 – 144, 2017.

[23] D. Morin, B.L. Kaarstad, B. Skajaa, O.S. Hopperstad, and M. Langseth. Testing and modelling of stiffened aluminium panels subjected to quasi-static and low-velocity impact loading. *International Journal of Impact Engineering*, 2017.

[24] User manual - eCorr - Digital Image Correlation Tool. `https://www.ntnu.edu/kt/ecorr`. Accessed: 2018-05-03.

[25] E. Fagerholt, T. Børvik, and O.S. Hopperstad. Measuring discontinuous displacement fields in cracked specimens using digital image correlation with mesh adaptation and crack-path optimization. *Optics and Lasers in Engineering*, 51(3):299 – 310, 2013.

[26] F. Barlat, H. Aretz, J.W. Yoon, M.E. Karabin, J.C. Brem, and R.E. Dick. Linear transfomation-based anisotropic yield functions. *International Journal of Plasticity*, 21(5):1009 – 1039, 2005.

[27] *ABAQUS 6.14 Documentation*. Dassault Systèmes, Providence Road, Rhode Island, 2014.

[28] *LS-OPT User's Manual, version 5.2*. Livermore Software Technology Corporation, Livermore, California, 2015.

[29] H. Hooputra, H. Gese, H. Dell, and H. Werner. A comprehensive failure model for crashworthiness simulation of aluminium extrusions. *International Journal of Crashworthiness*, 9(5):449–464, 2004.

[30] A. Reyes, C. Dørum, O. S. Hopperstad, M. Langseth, O-G. Lademo, and M. Eriksson. Validation study of failure prediction in crash analysis. In *9th International Conference on Computational Structures Technology*, Athens, Greece, 2009. Civil-Comp Proceedings.

[31] A. G. Hanssen, T. Auestad, T. Tryland, and M. Langseth. The kicking machine: A device for impact testing of structural components. *International Journal of Crashworthiness*, 8(4):385–392, 2003.

[32] M. Costas, D. Morin, M. Langseth, L. Romera, and J. Díaz. Axial crushing of aluminum extrusions filled with PET foam and GFRP. An experimental investigation. *Thin-Walled Structures*, 99:45 – 57, 2016.

[33] M. Costas, D. Morin, M. Langseth, J. Díaz, and L. Romera. Static crushing of aluminium tubes filled with PET foam and a GFRP skeleton. Numerical modelling and multiobjective optimization. *International Journal of Mechanical Sciences*, 131-132:205 – 217, 2017.

[34] M. Kristoffersen, T. Børvik, I. Westermann, M. Langseth, and O.S. Hopperstad. Impact against X65 steel pipes – An experimental investigation. *International Journal of Solids and Structures*, 50(20):3430 – 3445, 2013.

[35] J. K. Sønstabø, D. Morin, and M. Langseth. Static and dynamic testing and modelling of aluminium joints with flow-drill screw connections. *International Journal of Impact Engineering*, 115:58 – 75, 2018.

[36] T. Børvik, A.H. Clausen, M. Eriksson, T. Berstad, O.S. Hopperstad, and M. Langseth. Experimental and numerical study on the perforation of AA6005-T6 panels. *International Journal of Impact Engineering*, 32(1):35 – 64, 2005.